Bioimage informatics

# Fully Unsupervised Symmetry-Based Mitosis Detection in Time-Lapse Cell Microscopy

**Topaz Gilad[1], Jose Reyes[2], Jia-Yun Chen[2], Galit Lahav[2] and Tammy Riklin Raviv[1,*]**

[1] Department of Electrical and Computer Engineering and the Zlotwoski Center for Neuroscience, Ben-Gurion University of the Negev, Israel

[2] Department of Systems Biology, Harvard Medical School, U.S.A.

*To whom correspondence should be addressed.

Associate Editor: XXXXXXX

Received on XXXXX; revised on XXXXX; accepted on XXXXX

## Abstract

**Motivation:** Cell microscopy datasets have great diversity due to variability in cell types, imaging techniques, and protocols. Existing methods are either tailored to specific datasets or are based on supervised learning, which requires comprehensive manual annotations. Using the latter approach, however, poses a significant difficulty due to the imbalance between the number of mitotic cells with respect to the entire cell population in a time-lapse microscopy sequence.

**Results:** We present a fully unsupervised framework for both mitosis detection and mother-daughters association in fluorescence microscopy data. The proposed method accommodates the difficulty of the different cell appearances and dynamics. Addressing symmetric cell divisions, a key concept is utilizing daughters' similarity. Association is accomplished by defining cell neighborhood via a stochastic version of the Delaunay triangulation and optimization by dynamic programming. Our framework presents promising detection results for a variety of fluorescence microscopy datasets of different sources, including 2D and 3D sequences from the Cell Tracking Challenge.

**Availability:** code is available in github: github.com/topazgl/mitodix

**Contact:** topazg@post.bgu.ac.il; rrtammy@ee.bgu.ac.il

**Supplementary information:** Supplementary material is available at *Bioinformatics* online.

## 1 Introduction

Nowadays modern microscopes enable biologists to conduct observations on living cells throughout time. A main process of interest is mitosis, in which a cell undergoes nucleus division (Alberts *et al.*, 2015). The study of mitosis has a substantial impact on many biomedical fields such as microbiology and cancer research (Dogra *et al.*, 2017; Hein *et al.*, 2017). Thanks to the ongoing development in acquisition techniques and storage devices, the available datasets are large and diverse, which makes manual annotation impracticable. Thus, there is a demand for robust automatic tools, that can provide reproducible objective results (Zimmer *et al.*, 2006).

Developing generally applicable frameworks for mitosis detection is challenging due to the huge variability in cell appearance caused by the differences in datasets, the chemical compounds used, and the microscopy imaging technique. Cells' dynamics can therefore provide a significant cue for mitosis detection. Numerous methods exploit time-lapse microscopy dynamics and use cell tracks to detect cell divisions. In the work of Thirusittampalam *et al.* (2013), a mother cell is associated with only one of the daughter cells, afterwards performing backward tracking to connect the two daughters with the mother cell. In Arbelle *et al.* (2018) an appearance of a new cell, which is not located at the frame's edge, implies a possible mitotic event. Huh *et al.* (2012) suggest a tracking based method for free-floating cells based on Hidden Conditional Random Fields (HCRF). A drawback of these methods is that the success of mitosis detection greatly depends on the tracking performance. Moreover, an excessive computational complexity is required, when the purpose of the analysis is limited to the study of cell divisions, e.g., detection of changes in proliferation rate related to mitosis bursts (Sullivan and Epstein, 1963) or mitotic waves (Vergassola *et al.*, 2018), which may not necessarily require (to some extent) individual cell tracking.

As the appearance of dividing cells may change dramatically, most current approaches use supervised machine learning (ML) algorithms to detect mitotic events based on the visual and temporal traits. In these works feature selection is followed by a trained classifier (Li *et al.*, 2010, Liu *et al.*, 2012, Tashk *et al.*, 2015). In the work of Tonti *et al.* (2015) an unsupervised approach is designed based on textural features of a specific dataset using k-means clustering. These methods are designed for specific cell types, usually based on a carefully selected set of distinguishing features and therefore may not apply to general cases. Other supervised ML approaches use implicit features (Liu *et al.*, 2017a, Wan *et al.*, 2017). Neural Networks (NN) enable learning the features directly from the data. In the context of mitosis detection, many NN-based algorithms are designed for the public datasets for histologic tumor grading of breast cancer: AMIDA13 (Veta *et al.*, 2015), MITOS (Roux *et al.*, 2013), and MITOS-ATYPIA (Roux *et al.*, 2014). Unlike those single-image datasets, time-lapse microscopy sequences include cell dynamics, which is a plausible feature in mitotic detection. While the works of Nie *et al.* (2016) and Chen *et al.* (2016) do incorporate the temporal domain, hundreds of annotated mitotic events for training are required. Recently, Phan *et al.* (2017) suggested an unsupervised learning method based on an NN architecture applied to phase-contrast microscopy images. The network outputs irregularities in the dataset, followed by clustering to extract mitotic cells. While being an interesting approach, the fact that mitotic events localization is based on pixel-level intensity enhancement limits its applicability.

Unlike supervised and other unsupervised ML techniques, the proposed contribution does not rely on labeled data, nor is it tailored to a specific fluorescence-microscopy dataset. Considering symmetrical cell divisions, the proposed fully unsupervised framework exploits daughters' similarity as a common trait. This key concept is generally applicable, given that the daughters are captured at the Anaphase stage, after the Deoxyribonucleic Acid (DNA) material divides, where the two daughter cells are approximately identical. Mother-daughters association is accomplished by encoding cells' neighborhood via stochastic Delaunay triangulation and candidate triplet association optimized via linear programming.

The rest of the paper is organized as follows: The main contributions of the proposed approach are outlined in Section 2. The method is further detailed in Section 3, where we present two biologically-driven key elements on which it is founded: division symmetry (daughters' similarity) and mother-daughters dissimilarity. In addition, we introduce a stochastic variant of the Delaunay triangulation to detect spatially neighboring cells and an integer programming formulation for global frame optimization. Implementation and experiments are presented in Section 4. Concluding remarks and suggestions for future work are given in Section 5.

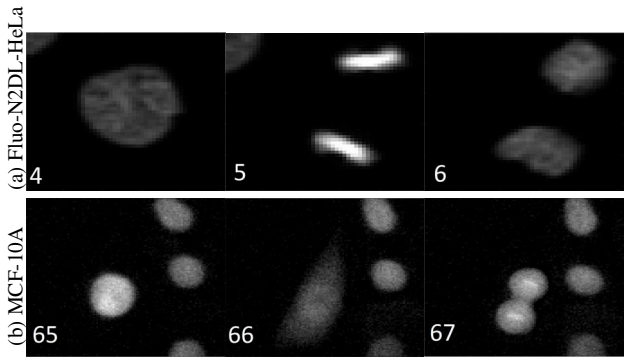


**Fig. 1.** Cell division in two different datasets: Each row displays time-lapse imagery of a cell division from a different dataset: (a) Fluo-N2DL-HeLa cells (Ulman et al., 2017), (b) MCF-10A cells courtesy of Albeck & Brugge. Frame number is shown at the bottom left of each image.

## 2 Proposed approach

The challenge of unsupervised mitosis detection is addressed using three modular stages: First, mitotic cell candidates are identified based on local spatio-temporal intensity differences. Second, candidate daughters are examined using symmetry estimation. Third, mother-daughters association is performed by solving an integer programming optimization problem.

In a previous work symmetry has been exploited to detect mitotic events (Gilad *et al.*, 2015). The proposed framework presents three, additional main contributions: First, we define a similarity measure that incorporates sensitivity to dynamic range differences between cells' instances. This measure is calculated using a vector form for the weighted Pearson correlation coefficient (detailed in Section 3.3). We employ it both for symmetry estimation (Section 3.5) and spatio-temporal dissimilarity identification; Second, we suggest a stochastic version of the Delaunay triangulation to address possible ambiguities (Section 3.4). The proposed triangulation is used for neighborhood cells calculations when pairing candidate daughter cells; Third, we formulate the constraint of a linear programming optimization problem to match pairs of cells in one frame to a single cell in the previous frame and use it to find a frame-wise optimal solution of both daughter-pairing and mother-daughters associations (as explained in Section 3.7).

Consider the pairs of consecutive frames, displayed in Fig. 1; each row is showing a mitosis event of a different cell type acquired at a different frame rate. The proposed algorithm accommodates the difficulty of the diversity in cell visual and temporal features without making a specific assumption on the shape or the texture of a mother cell. Moreover, as opposed to many algorithms, it does not require user-annotated data. Instead, as the majority of cells undergo symmetrical divisions, mitosis is detected based on daughter cells similarity right after the division. Using symmetry for mitosis detection has been suggested in Li *et al.* (2010), and applied to elongated cells. Nevertheless, the symmetry axis was determined based on the major axis of the mother cell, which is generally not as pronounced. In contrast, the proposed framework is based on our observation that the symmetry axis is orthogonal to the virtual straight line that connects the centroids of the two daughter cells.

We demonstrate the applicability of the method proposed for two- and three-dimensional fluorescence microscopy sequences for cells undergoing symmetric divisions. Specifically, we use publicly available data of the Cell Tracking Challenge: `http://www.celltrackingchallenge.net` - i.e., Fluo-N2DL-HeLa, Fluo-N2DH-SIM+, and Fluo-N3DH-SIM+ (Maska *et al.*, 2014; Ulman *et al.*, 2017) and private datasets including MCF-10A (Kamentsky *et al.*, 2011) and Retinal Pigmented Epithelial (RPE) cell sequences. Given that most cell divisions are symmetric, daughters' similarity is a key element of the proposed approach and therefore aberrant divison events cannot be properly handled. Accounting also for mother-daughters association, clustered cells that cannot be readily separated cannot be grouped as mitotic triplets using our method. While the underlying assumptions may appear to be restrictive, we note that our method is fully unsupervised and does not require labeled training data or any training process. Moreover, we used the same set of parameters in all experiments. Promising mitosis detection results were obtained for the different fluorescence microscopy datasets and for different temporal and spatial resolutions of the sequences, in particular the ability to enhance a tracking-based approach is shown.

# 3 Methods

## 3.1 Overview

We aim to detect mitotic events in a completely unsupervised manner, without parameter tuning while accommodating a variety of fluorescence microscopy datasets. Instead of using annotated mitosis examples, the following assumptions are made: 1. Mitotic events are characterized by spatio-temporal intensity differences; 2. Only symmetric cell divisions are addressed; 3. Cell segmentations or alternatively cells' centers of mass (COMs) are provided. In the latter case, cell segmentation can be approximated, for example by a disc given the cells' average radius.

The general flow of the proposed mitosis detection framework is displayed in Fig. 2. The input to the algorithm is a fluorescence microscopy frame sequence (Fig. 2a) and the respective cells' segmentations (or cells' COMs). Input frames are partitioned into patches (see Section A.1, Appendix), centered at the cells' COMs (calculated based on the input segmentation), and paired with the spatially corresponding patch in the consecutive frame. The proposed algorithm is based on the following stages:

- **Mitotic Candidates Identification (Fig. 2b):** The first stage is founded on patch-based spatio-temporal intensity differences indicating cells that undergo some visual change between two consecutive frames. Rather than setting a manually tuned threshold on the dissimilarity measure (defined in Section 3.3) between pairs of image patches, we look at the dissimilarity distribution (i.e., normalized histogram) and use the Otsu (1979) method to set the threshold automatically. This is made possible since the distribution appears to be bi-modal, roughly distinguishing between mitotic and non-mitotic cells. Note that at this preliminary stage we can accept false positives (e.g., patches that are subject to significant temporal changes due to exceptional cell dynamics) but false negatives (missed true mitotic cells) directly decrease the final performances. Nevertheless, this filtering step is essential as the following steps are computationally expensive and should not be applied to the entire population.
- **Neighborhood Association (Fig. 2c):** Next, we use a stochastic version of the Delaunay triangulation, as introduced in Section 3.4, for the construction of mother-daughters triplets based on spatial proximity of mothers and daughters.
- **Daughters' Symmetry Evaluation (Fig. 2d):** We use the dissimilarity measure defined in Section 3.3 to evaluate daughters' symmetry, following symmetry axis extraction presented in Section 3.5.
- **Clustering Analysis (Fig. 2e):** We then consider mother-daughters dissimilarity and daughters similarity and perform clustering analysis (see Section 3.6). This step, as before, is done in an unsupervised manner, providing for each triplet the estimated likelihood to be a mitotic event.
- **Mitotic Events Selection (Fig. 2f):** Finally, we solve an integer programming problem to discard contradicting triplets (i.e., a daughter cell with two mothers etc.), as detailed in Section 3.7. The output consists of birth frame number, centroid of the mother and daughter cells, and the estimated confidence of each mitotic event.

The key concepts of the suggested algorithm are presented in the following Section.

## 3.2 General Notations

We denote the input sequence of intensity gray level microscopy images by $\{\mathbf{I}_t\}_{t=1}^{T}$ , where $T$ is the total number of frames in the input sequence, $\mathbf{I}_t : \Omega_t \to \mathbb{R}$ is the image related to frame $t$, and $\Omega_t$ is a two-dimensional image domain. We assume that the binary segmentation of each frame $I_t$ is given and denoted as follows: $\mathbf{L}_t : \Omega_t \longmapsto \{0,1\}$ where "0" is assigned to background pixels and "1" to cell pixels. We denote by $c_{t,i}$ the $i^{\text{th}}$ cell instance in frame $t$, where $i = 1, ..., C_t$ and $C_t$ is the total number of cells in that frame. We define by $\omega_{t,i} \subseteq \Omega_t$ the domain of the bounding box of $c_{t,i}$.

## 3.3 Similarity Measure

We use a weighted form of the Pearson correlation coefficient similarity measure (Pearson, 1895; Abdullah, 1990) for mitotic candidate identification via temporal patch-based dissimilarity and for evaluation of daughter cells' similarity. To roughly align the two compared cell patches, similarity transformation (rotation and translation) prior to the calculation of the correlation coefficients is applied. In addition, the contribution of each pixel to the measure's calculation is weighted to reduce the influence of background pixels, in particular those related to neighboring cells.

For simplicity we omit the subscript $t$, which denotes the time index. Let $\mathbf{y}_1, \mathbf{y}_2 \in \mathbb{R}^N$ be vectorized forms of two image patches, where $N$ is the number of pixels in a patch. We denote by $\mathbf{w}^T \in (0,1)^N$ the corresponding weight vector such that: $\mathbf{w}^T\mathbf{w} = 1$. The covariance is calculated as:

$$Cv_{i,j} \triangleq Cov^w(\mathbf{y}_i, \mathbf{y}_j) = \mathbf{y}_i^T \mathbf{W} \mathbf{y}_j \tag{1}$$

where the matrix $\mathbf{W}$ is constructed s.t. the weight vector $\mathbf{w}$ is its diagonal and its non-diagonal entries are zeros.

The correlation coefficient is therefore:

$$C_{1,2}^w \triangleq Corr^w(\mathbf{y}_1, \mathbf{y}_2) = \frac{Cv_{1,2}}{\sqrt{Cv_{1,1}Cv_{2,2}}} \tag{2}$$

Note that since our case is mono-modal, two cell images should have the same intensity scaling to be considered similar. We, therefore, use the reflective correlation, where the samples are not centered. To increase the penalty for intensity scaling differences, we also use the ratio between the images' weighted expectations. We define the weighted mean $\mu_i^w$, where $i = 1, 2$, as follows:

$$\mu_i^w = \mathbf{w}^T \mathbf{y}_i \tag{3}$$

The ratio is therefore:

$$M_{1,2}^w \triangleq \min(\mu_1^w, \mu_2^w) / \max(\mu_1^w, \mu_2^w) \tag{4}$$

Image intensity can be attributed to cells' chromatin, which is being labeled in the datasets used. Thus, considering the intensity ratio also has a biological incentive since chromatin-bound or diffused fluorescent proteins distribute to the two daughter cells upon division (Downey *et al.*, 2011).

We define the similarity measure as follows:

$$s_{1,2}^w \triangleq p(\mathbf{y}_1 = \mathbf{y}_2 \mid \mathbf{w}) = \frac{1}{2}\left(C_{1,2}^w + 1\right) \cdot M_{1,2}^w \tag{5}$$

Note that the range of a correlation coefficient is $[-1, 1]$. In mono-modal cases, negative correlation corresponds to strong asymmetry. $C_{1,2}^w$ is calculated according to Eq. (2). $M_{1,2}^w$ is calculated as in Eq. (4).

In Gilad *et al.* (2015) Gaussian weights were used. We now suggest a more informative weighting that incorporates the shape prior. A straightforward choice for a shape prior would be the input binary segmentation $\mathbf{L}$, which partitions the image domain into two classes: cell pixels $\omega_c \subseteq \Omega$ and background pixels $\omega_b = \Omega \setminus \omega_c$. Assuming uncertainty of $\mathbf{L}$, we use $\mathbf{H} : \Omega \longmapsto [0,1]^{\mathrm{N}}$ to map the image pixels to a probabilistic space.

Consider a pixel $\mathbf{x} = (x, y) \in \Omega$ as a random 2D vector. Assuming equal a priori probabilities, since no a priori knowledge exists, we define the log likelihood ratio decision boundary:

$$\varphi(\mathbf{x}) \triangleq \log \frac{p(\mathbf{x} \in \omega_c)}{p(\mathbf{x} \in \Omega \setminus \omega_c)} \underset{\omega_b}{\overset{\omega_c}{\gtrless}} 0 \tag{6}$$

The above decision rule achieves maximal a posteriori probability (MAP) according to Bayes, for known conditional probability function

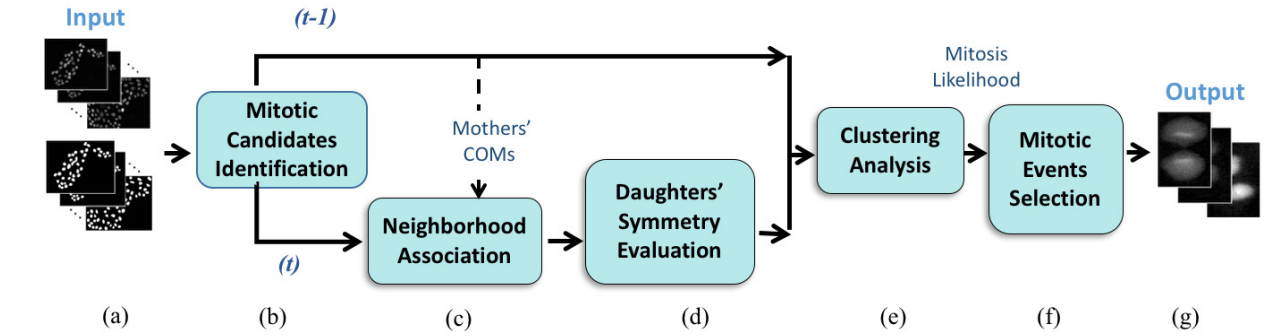


**Fig. 2.** Block Diagram of the general flow of the proposed framework. (a) Input includes a fluorescence microscopy frame sequence and the respective cells' segmentations or cells' COMs). (b) Each frame is partitioned into patches based on the cells' COMs. Initial mitotic cells candidates are extracted based on spatio-temporal difference between corresponding, consecutive frame patches (Section 3.3). (c) For each candidate mother, potential daughters are paired according to neighborhood encoded via Stochastic Delaunay triangulation (Section 3.4). (d) Symmetry axis is retrieved for each pair of candidate daughters and similarity between them is calculated (Section 3.5). (e) Based on daughters' similarity and mother-daughters' dissimilarity, clustering analysis is performed to assign for each mitotic candidate triplet the probability to be a true mitotic event (Section 3.6). (f) Integer programming optimization is used to filter-out contradicting mitosis candidates (Section 3.7). (g) The output consists of birth frame number, centroid of the mother and daughter cells, and the estimated probability (indicating uncertainty) of each mitotic event.

$p\left(\mathbf{x} \in \omega_c\right)$ and equal a priori probabilities. The resulting probability map is:

$$\mathrm{H}\left(\varphi(\mathbf{x})\right) \triangleq p\left(\mathbf{x} \in \omega_c\right) = \left[1 + \exp\left(-\frac{\varphi\left(\mathbf{x}\right)}{\varepsilon}\right)\right]^{-1} \tag{7}$$

where, $\varepsilon$ defines the uncertainty. In the spirit of Pohl *et al.* (2006) and Riklin Raviv *et al.* (2010), the decision rule in Eq. (6) is estimated by a Sign Distance Function (SDF). This is analogous to an approximation of the conditional density function based on Euclidean distance from the cells' boundary. Denote the boundary of cell $c_i$ segmentation as $\partial\omega_i \in \Omega$. The SDF $\varphi_i\left(\mathbf{x}\right) : \Omega \longmapsto \mathbb{R}$ associated with the binary segmentation of the $i^{\text{th}}$ cell is defined as follows:

$$\varphi_i\left(\mathbf{x}\right) = \begin{cases} d\left(\mathbf{x}, \partial\omega_i\right) & \mathbf{x} \in \omega_i \\ -d\left(\mathbf{x}, \partial\omega_i\right) & \mathbf{x} \in \Omega \setminus \omega_i \end{cases} \tag{8}$$

where $d\left(\mathbf{x}, \partial\omega_i\right)$ is the minimal Euclidean distance between a pixel $\mathbf{x}$ and a boundary pixel. The weight vector $\mathbf{w}_i$ that is used for the weighted correlation calculation in Eq. (2) is defined by $\mathrm{H}(\varphi_i)$ normalized s.t. ${\mathbf{w}_i}^T\mathbf{w}_i = 1$. The process is illustrated in Fig. 3.

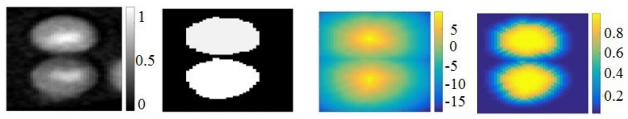


(a) Image (b) Segmentation (c) SDF (d) probability map

**Fig. 3.** Weights matrix - Fuzzy Segmentation: (a) Gray level intensity image. (b) Binary segmentation. (c) Sign distance function (SDF) of the binary segmentation presented in (b). (d) Probability map.

### 3.4 Neighborhood association via Delaunay triangulation

We assume that mitosis daughter cells are adjacent and symmetrical to one another right after separation. In this section, we will define the concept of neighborhood between candidate daughter cells. Daughters' symmetry is addressed in the next section.

To define pairing between candidate daughter cells, we represent each frame by a sparse graph, where the nodes are defined by cells' COMs and the edges are defined by our stochastic version of the Delaunay triangulation (Delaunay, 1934). Candidate daughter cells are connected via an edge.

Encoding local cells' neighborhood connections using triangulation was previously suggested in several cell tracking algorithms (Li *et al.*, 2010; Liu *et al.*, 2010, 2011; Thirusittampalam *et al.*, 2013; Liu *et al.*, 2016, 2017b), mainly for its stability in the presence of cell migration and division (illustrated in Fig. A.3.a, see Appendix). Moreover, triangulation does not require prior knowledge regarding the number of neighbors as in k-Nearest Neighbor.

The Delaunay triangulation is defined s.t. no node is inside any triangle circumcircle. The obtained diagram maximizes the minimal angle of all triangles (de Berg *et al.*, 2008); thus the triangles tend to equiangularity. Therefore, narrow thin (sliver) triangles are avoided and local structures are achieved. This implies that changes in the nodes have local influence. This property is especially important when encoding live cells' positions.

Nevertheless, the Delaunay triangulation is ambiguous when more than three points (nodes) lie on the same circle. In these cases possible "true" edges could be missed and the entire constellation is sensitive to noise. To address this limitation we suggest a stochastic version of the triangulation. The triangulation is recalculated in an iterative manner, where at each iteration the COMs are perturbed by an additive noise with a truncated Gaussian distribution. The additive noise reflects the uncertainty of the cell's COMs due to segmentation inaccuracy. It is set such that the distance between the original and the perturbed COM is smaller than the distance between neighboring COMs. For further details refer to the online appendix. The final set of edges in the resulting graph is the union of all edges found in each of the iterations. This reduces the number of mis-detected edges. Fig. A.3.b (see Appendix) illustrates the scenario, where the resulting new edges are marked in red. More details including assessment of the algorithm's convergence can be found in Section B in the online appendix.

### 3.5 Symmetry axis extraction

Daughter cells are assumed to have bilateral symmetry right after division. We expect that if such symmetry exists, the symmetry axis is perpendicular to the straight line that connects the COMs of the candidate daughter cells and intersects its center. Let us consider a sub-image $\mathbf{I}_{t,i,j} : \omega_{t,i,j} \mapsto \mathbb{R}$, where $\omega_{t,i,j} \subseteq \Omega_t$ contains the pixels of both candidate daughter cells $c_{t,i}$ and $c_{t,j}$ in frame $t$. To test symmetry, we wish to align the sub-image's main axis (w.l.o.g. the horizontal axis) with the potential symmetry axis. We start with rotating the sub-image according to the cells' COMs. However, recall that we cannot assume that the input segmentation, and therefore the respective COMs, are accurate. We therefore further adjust the alignment in the spirit of Riklin Raviv *et al.* (2009) as follows. For simplicity we omit the $t, i, j$ indexing. Let us denote

by $\boldsymbol{\theta} = (\theta_1, \theta_2, \theta_3)^T = (\tau_x, \tau_y, \alpha)^T$ the vector of translation $(\tau_x, \tau_y)$ and rotation angle $\alpha$ of the similarity transformation matrix $\mathbf{R}_{\boldsymbol{\theta}}$.

Our aim is to find the transformation parameters $\boldsymbol{\theta}$ that minimize the loss between the 2D image matrix $\mathbf{I}$ and its symmetrical counterpart $\mathbf{I}^{ud}$, which is obtained by up-down reflection. Let us denote by $\mathbf{y}$ and $\mathbf{y}^{ud}$ the vector representation of $\mathbf{I}$ and $\mathbf{I}^{ud}$, respectively. Let $\mathbf{y}^{ud}$ and $\mathbf{T}_{\boldsymbol{\theta}}\mathbf{y}$ be the vectorial representations of $\mathbf{I}^{ud}$ and the matrix obtained following transformation of the original sub-image $\mathbf{I}$ by $\mathbf{R}_{\boldsymbol{\theta}}$, respectively. We use the weighted Mean Square Error (MSE) as our loss function:

$$L\left(\mathbf{y} \mid \mathbf{w}, \boldsymbol{\theta}\right) = \left(\mathbf{y}^{ud} - \mathbf{T}_{\boldsymbol{\theta}}\mathbf{y}\right)^T \mathbf{W} \left(\mathbf{y}^{ud} - \mathbf{T}_{\boldsymbol{\theta}}\mathbf{y}\right), \qquad (9)$$

where the matrix $\mathbf{W}$ is constructed s.t. the weight vector $\mathbf{w}$ (see Section 3.3) is its diagonal and its non-diagonal entries are zeros. Our objective is to solve the following constrained optimization problem:

$$\widehat{\boldsymbol{\theta}} = \underset{\boldsymbol{\theta}\ s.t.\ \theta_k \in [a_k, b_k]}{\arg\min}\ L\left(\mathbf{y} \mid \mathbf{w}, \boldsymbol{\theta}\right) \qquad (10)$$

where $[a_k, b_k]; k = 1, ..., 3$ defines the valid range of transformation parameters (based on cell size and other factors), as detailed in the online appendix. As shown in Riklin Raviv *et al.* (2009), the orientation of the symmetry axis with respect to the coordinate system of $\mathbf{I}$ is $\frac{\widehat{\theta}}{2}$. This concept is illustrated in Fig. A.1 (see online Appendix). We next calculate the similarity (based on Eq. (5)) between the daughters' sub-images, obtained by a reflection along the retrieved symmetry axis, followed by bicubic interpolation.

### 3.6 Mother-daughters associations

Candidate mitotic event is defined by a triplet of a candidate mother cell in frame $t-1$ and a pair of candidate daughter cells in frame $t$. Each candidate event is represented by two features: candidate daughters' symmetry and mother-daughters' similarity. The first feature, i.e., the likelihood that two cells are mitotic daughters, is calculated using the similarity measure from Eq. (5) following the process described in Section 3.5. Mother-daughters' similarity $\mathcal{S}_{m,1,2}$ is calculated as follows:

$$\mathcal{S}_{m,1,2} \triangleq max(s_{1,m}, s_{2,m}) s_{1,2,m} \qquad (11)$$

where $s_{i,m},\ i = 1, 2$ are the similarity measures between the candidate mother and the $i^{\text{th}}$ daughter, calculated according to Eq. (5) and $s_{1,2,m}$ is the similarity between the patch consisting of both daughters and the candidate mother patch. The second similarity addresses over-segmentations in which one cell is erroneously segmented as two.

The mitotic cluster is assumed to be Normally distributed in the constructed 2D feature space. This assumption is assessed empirically; see for example Fig. 6. Let $V_0, V_1$ denote the mitotic and non-mitotic clusters, respectively. We use the Expectation Maximization (EM) algorithm (Dempster *et al.*, 1977) in order to find the distribution parameters $(\mu_k, \boldsymbol{\Sigma}_k), k = 0, 1$ and the a priori probabilities $P_k$. The cluster with highest average value of the daughters' symmetry feature is chosen as the mitotic cluster.

The feature vector of the $i^{th}$ mitotic candidate is denoted by $\mathbf{v}_i$. The a posteriori probability is estimated based on the mitotic cluster membership of the feature vector (Bezdek and Dunn, 1975; Gath and Geva, 1989):

$$l_i \triangleq p(V_0|\mathbf{v}_i, \mu_k, \boldsymbol{\Sigma}_k, P_k) = \frac{(d_{0,i})^{-1}}{\sum_{k=0}^{1} (d_{k,i})^{-1}} \qquad (12)$$

where, $d_{k,i}$ is the exponential distance:

$$d_{k,i} \triangleq \frac{1}{P_k} |\boldsymbol{\Sigma}_k|^{\frac{1}{2}} \exp\left[\frac{1}{2}(\mathbf{v}_i - \mu_k)^T \boldsymbol{\Sigma}_k^{-1} (\mathbf{v}_i - \mu_k)\right] \qquad (13)$$

A cell instance $c_{t,i}$ cannot be simultaneously a mother of a mitotic event in frame $t+1$ and a daughter of another event in frame $t$. Such contradictions are resolved by selecting the candidate triplets that are most probable.

### 3.7 Mitotic decision using integer programming

The feature space of mitotic candidates holds contradicting hypotheses. Given a set of candidate mitotic events associated with a frame $t$, we look for an optimal subset, subject to the following constraints: 1. Each cell in frame $t-1$ can be a mother of a single mitotic event in frame $t$ at most; 2. Each cell in frame $t$ can be a daughter of a single mitotic event at most; 3. The number of mitotic events in a single frame should be limited.

In order to meet these constraints we generalize the binary integer programming optimization problem (Nemhauser and Wolsey, 1989) to associate a pair of items in one group with a single item in another. Integer programming was previously suggested for one-to-one cell association (as in Li *et al.*, 2010; Merouane *et al.*, 2015) for non-mitotic cells. We define the likelihood vector by $\mathbf{l} = \left(l_1, ..., l_Q\right)^T$, where $l_j$ is the likelihood of the $j^{\text{th}}$ candidate in frame $t$ (see Eq. (12)), and $Q$ is the total number of candidate triplets in the frame. We wish to solve the following optimization problem:

$$\hat{\mathbf{q}} = \underset{\mathbf{q}}{\arg\max}\ \mathbf{l}^{\mathrm{T}}\mathbf{q}\ \ s.t.\ \ \mathbf{q} \in \{0, 1\}^Q, \quad \mathbf{A}\mathbf{q} \leq \mathbf{b} \qquad (14)$$

where $\mathbf{q}$ is an indicator vector, i.e., its $j^{\text{th}}$ entry equals 1 if the $j^{\text{th}}$ candidate is chosen. Let $K_D, K_M$ be the number of candidate daughters in frame $t$ and candidate mothers in frame $t-1$, respectively. We set $K = K_D + K_M$. The vector $\mathbf{b} = (b_1, ..., b_K)^T$ is constructed, s.t. each cell can be part of a single candidate triplet at most, thus $b_k = 1,\ \forall k$. We construct the matrix $\mathbf{A} \in \{0, 1\}^{K \times Q}$, s.t. each column $j$ represents the triplet (mother and daughters) that defines the $j^{\text{th}}$ mitosis candidate. The $i^{\text{th}}$ row in $\mathbf{A}$ represents all candidate triplets in which cell $i$ takes part. Specifically, denote the $j^{\text{th}}$ triplet by $\left(c_{t,d_1^j}, c_{t,d_2^j}, c_{t-1,m^j}\right)$, where $\left(d_1^j, d_2^j\right)$ are the indices of the $j^{\text{th}}$ candidate's daughters and $m^j$ is the index of the candidate mother cell. The matrix element $[\mathbf{A}]_{ij}$ is set as follows:

$$[\mathbf{A}]_{ij} = \begin{cases} 1; & i = d_1^j \ or\ i = d_2^j, \quad 1 \leq i \leq K_D \\ 1; & i = m^j + K_D, \qquad K_D < i \leq K \\ 0; & \text{otherwise} \end{cases} \qquad (15)$$

Note that $\mathbf{A}$ is constructed s.t. each column sums to 3. An example illustration is available in the online appendix.

## 4 Experiments

### 4.1 Datasets

We tested our method on different time-lapse fluorescence microscopy datasets (2D and 3D). The cells' image sequences were acquired with either nucleus labeled by iRFP fused to NLS (nuclear location signal) or fluorescent protein fused to histone H2B. Data include the publicly available Cell Tracking Challenge datasets: `http://www.celltrackingchallenge.net` detailed in (Ulman *et al.*, 2017): Fluo-N2DL-HeLa and the synthesized Fluo-N2DH-SIM+ and Fluo-N3DH-SIM+ (Svoboda and Ulman, 2017) datasets, as well as private datasets: MCF-10A and Retinal Pigmented Epithelial (RPE) cells immortalized with overexpression of telomerase. Further details on the different image sequences such as the number of frames, frame rate, and average number of cells per frame are presented in Table 3.

### 4.2 Evaluation measures

We quantitatively evaluated the proposed algorithm using for all datasets, except for the simulated ones, manually annotated mitosis events, considered as Ground Truth (GT). Since Fluo-N2DH-SIM+ and Fluo-N3DH-SIM+ are computer-generated image data, their annotations were inherently provided by a simulation system. We note that the Fluo-N2DL-HeLa, Fluo-N2DH-SIM+, and Fluo-N3DH-SIM+ datasets are originally

intended for the cell tracking challenge and not for the specific task of mitosis detection. We, therefore, could only evaluate our method on their publicly available training sets. Since our method is fully unsupervised we could use the training set for testing.

Let a GT mitosis event be defined by the "birth" frame $t'$ and the COMs of the GT mother $\mathbf{x}'_m$ and daughters $(\mathbf{x}'_{d_1}, \mathbf{x}'_{d_2})$. A true positive ($TP$) detection is defined as a candidate in frame $t$ that meets the criteria in Eq. (16), where the triplet candidate COMs are $(\mathbf{x}_m, \mathbf{x}_{d_1}, \mathbf{x}_{d_2})$.

$$\begin{cases} |t' - t| \leq 1 \\ \parallel \mathbf{x}'_l - \mathbf{x}_l \parallel \leq \Re\,, \; l = d_1, d_2, m \end{cases} \tag{16}$$

$\Re$ is average cell radius calculated based on input segmentation. Note that the TP criteria (Eq. (16)) require both spatio-temporal localization of the mitotic event and a correct association between mitotic mother and the pair of daughters. Detections that do not meet these strict criteria are considered False Positive ($FP$). Each candidate can only be assigned to one GT event and each GT event is only detected once. If more than a single candidate triplet meets the criteria in Eq. (16) for the same GT event (two adjacent mitotic candidate events), the one with the highest likelihood (Eq. (12)) is considered $TP$ and the others $FP$. Undetected mitosis events are defined as False Negatives ($FN$). All other events are defined as True Negatives ($TN$). In order to measure and compare detection performance we use the following golden standard metrics: True Positive Rate ($TPR$, also known as recall), Precision ($P$), False Positive Rate ($FPR$), and $F_1$ score:

$$\begin{cases} TPR(r) = \frac{TP(r)}{TP(r)+FN(r)}; \quad P(r) = \frac{TP(r)}{TP(r)+FP(r)} \\ F_1(r) = 2\frac{TPR(r)\cdot P(r)}{TPR(r)+P(r)}; \quad FPR(r) = \frac{FP(r)}{FP(r)+TN(r)} \end{cases} \tag{17}$$

where $r$ defines an operating point. The $F_1(r)$ score corresponds to the branching correctness (BC) measure, defined and used in (Bise *et al.*, 2011; Magnusson *et al.*, 2015; Ulman *et al.*, 2017) with time interval of one frame. The measure $\max F_1 \triangleq \max(F_1(r))$ is used for results assessment as well. In addition, we examine stability in performance over a range of possible operating points using the Receiver Operating Characteristic (ROC) graph (Powers, 2011) and calculating the area under the ROC curve (AUC). We note that the operating point for the initial stage of mitotic candidates identification is calculated automatically using Otsu (1979).

## 4.3 Experimental results

To assess the proposed method the following experiments were conducted: We first compared the proposed mitotic candidate identification phase with an alternative, principle component analysis (PCA) approach for detecting mitotic events as outliers, adapted from Jablonski *et al.* (2015). Next, we demonstrated the clustering obtained based on the candidate daughters' symmetry and mother-daughters' dissimilarity (Fig. 6). Mitotic detection results are then presented (Table 2). In addition we tested the robustness of the proposed algorithm to different temporal and spatial resolutions of the data, its sensitivity to the accuracy of cell segmentation, and a comparison to a tracking-based algorithm. Implementation details are available at the online supplementary appendix.

### 4.3.1 Mitotic candidates identification

We evaluated the preliminary stage of mitotic candidates identification by constructing precision w.r.t. TPR and ROC plots, based on the similarity (Eq. (5)) between consecutive corresponding image patches. For comparison, we used PCA of the patches to detect spatial anomalies that may indicate phenotypic appearance of mitosis. Fig. 4 displays the ROC plots and the precision w.r.t. TPR (red-ours, blue-PCA) for the Fluo-N2DL-HeLa02 sequence. The ROC's operating point is determined by the Otsu threshold presented as the dashed green line in Fig. 5. The AUC is the area under the ROC curve. $\max F1$ scores are the maximal $F_1$ scores obtained for each of the methods, using Eq. (17). Fig. 5 presents a patch-based histogram of temporal similarity for the Fluo-N2DL-HeLa02 sequence. The true mitotic events are marked in red (vs. blue). The threshold (dashed green line) is set automatically using the Otsu (1979) method. We note the approximately bi-modal distribution of mitotic vs. non-mitotic cells and the significantly lower number of below-threshold instances. The temporal intensity differences appear to be a significant cue, probably since the diffused fluorescent proteins or mother's chromatin (labeled in the analyzed data and manifested by enhanced image intensities) is distributed between its two daughter cells. The alternative PCA approach may be useful for non-fluorescence data. The AUC values and the $\max F_1$ scores for each of the tested datasets are presented in Table 1, showing the advantage of the proposed approach. Application of two-sample Kolmogorov-Smirnov test to the $F_1$ scores have shown a statistically significant difference (p-values $< 5\%$) for the compared sequences.

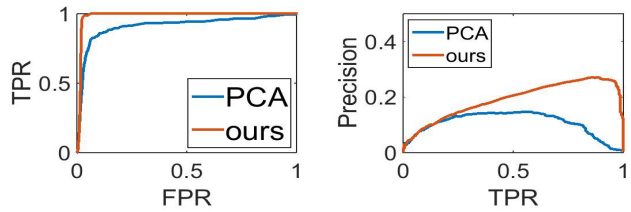


(a) ROC plot (b) Precision w.r.t. TPR

**Fig. 4.** ROC plots for identification of mitotic event candidates - Fluo-N2DL-HeLa02 example: (a) ROC plots, (b) Precision w.r.t. TPR plots. Both pairs of plots are based on data extracted from the Fluo-N2DL-HeLa02 sequence and obtained for the initial stage of mitotic candidates identification using the proposed patch-based spatio-temporal dissimilarity (red) and PCA for outliers detection (blue). The ROC's operating point is determined by the Otsu threshold presented as the dashed green line in Fig. 5. The AUC is the area under the ROC curve. $\max F1$ scores are the maximal $F_1$ scores obtained for each of the methods, using Eq. (17)

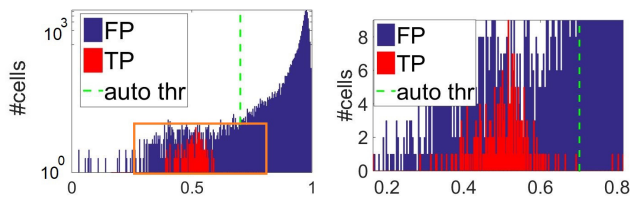


(a) Similarity histogram (b) Zoom-in

**Fig. 5.** Patch-based histogram of spatio-temporal similarity - Fluo-N2DL-HeLa02 example: (a) Spatio-temporal similarity histogram of Fluo-N2DL-HeLa02 consecutive corresponding image patches. The threshold (dashed green line) is automatically determined using Otsu (1979) to minimize intra-class variance. True mitotic events are marked in red, non-mitotic cells are marked in blue. Candidate mitotic cells are those below the threshold. (b) Zoom-in of the orange rectangle region shown in (a).

### 4.3.2 Mitotic events clustering

Associating mother-daughters triplets, each candidate event is represented by two features: daughters' symmetry and mother-daughters' similarity. Fig. 6 illustrates candidates scatter in this 2D features space for the HeLa01 sequence. The TP population, characterized by high daughters' similarity and low mother-daughters' similarity forms a condensed, approximately normally distributed cluster in the upper-left corner of the 2D plot.

### 4.3.3 Mitotic detection and mother-daughters association

Table 2 presents final results, including mother-daughters association performances. The measures are reported for the operating points that were set based on the thresholds calculated in the outlier detection stage (see Section 4.3.1). Even though there exists a significant imbalance between the number of mitotic events and the entire cell population, our algorithm displays high specificity. Moreover, although the algorithm is fully unsupervised with no manually tuned parameters, applicable

| Dataset | Ours AUC/max $F_1$ | PCA AUC/max $F_1$ |
|---|---|---|
| MCF-10A | 0.946 / 0.52 | 0.789 / 0.10 |
| Fluo-N2DL-HeLa01 | 0.986 / 0.58 | 0.902 / 0.26 |
| Fluo-N2DL-HeLa02 | 0.982 / 0.42 | 0.908 / 0.23 |
| RPE-01 | 0.945 / 0.35 | 0.848 / 0.03 |
| RPE-02 | 0.997 / 0.45 | 0.845 / 0.05 |
| RPE-03 | 0.932 / 0.57 | 0.667 / 0.01 |
| Fluo-N2DH-SIM+01 | 0.930 / 0.61 | 0.800 / 0.15 |
| Fluo-N2DH-SIM+02 | 0.940 / 0.50 | 0.720 / 0.12 |
| Fluo-N3DH-SIM+01 | 0.940 / 0.76 | 0.790 / 0.26 |
| Fluo-N3DH-SIM+02 | 0.900 / 0.74 | 0.760 / 0.19 |

**Table 1.** Initial mitotic mother candidates identification: Reported values are: (AUC / max $F_1$). AUC is the area under the ROC curve. max $F_1$ is the maximum F-measure of all possible working points (thresholds). The comparison is between the proposed mitotic candidate identification, based on spatio-temporal intensity differences and the PCA approach to detect outliers.

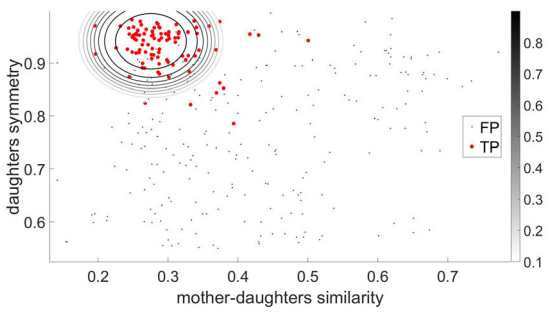


**Fig. 6.** Clustering: Candidate mother-daughters triplets are ranked in an unsupervised manner, based on the probability to be assigned to a mitotic events cluster. Each candidate triplet is represented by two features. The graph shows candidates scatter in the features space for the Fluo-N2DL-HeLa01 sequence, where true events are marked in red and false are marked in blue. Samples are clustered assuming multivariate normal distribution. The equiprobability contours of the estimated mitotic cluster are illustrated and color-coded, see color-bar on the right side.

sensitivity is demonstrated. Considering 3D data, we made the assumption that the cells divide in the x-y plane. While this assumption allows reduction of registration complexity, it may introduce errors. In general, for all datasets, we note that when a triplet contains a true mother and daughter and another false daughter - this type of error is counted twice, both as a false positive and false negative. Some of the other errors are due to over- or under-segmentation or when cells are missed completely due to low contrast with the background. Qualitative mitosis detection results are demonstrated in the videos that can be accessed using the link in https://github.com/topazGl/Mitodix.

#### 4.3.4 Robustness to segmentation quality

A main assumption in this framework is that the image sequences are provided along with cells' segmentation, or, at least, cells' COMs. To test the robustness of our method with respect to the accuracy of the segmentations, we replaced the binary segmentation mask that properly extracts cell boundaries with elliptical discs, centered at the respective cells' COMs and having similar scales. Results for the HeLa01 are reported in Table 2, see **HeLa-discs**. Note that the differences in all reported measures with respect to the Hela01 results with the complete segmentations (**Fluo-N2DL-HeLa01**) in Table 2 are negligible. We note, however, that cases in which two cells are mistakenly merged into a single connected component, or a single cell is labeled by two connected components, may degrade the performance significantly.

| Dataset | TP | FP | FN | FPR | $TPR$ | $P$ | $F_1$ |
|---|---|---|---|---|---|---|---|
| MCF-10A | 38 | 2 | 19 | 2.77E-04 | 0.68 | 0.95 | 0.78 |
| Fluo-N2DL-HeLa01 | 86 | 3 | 8 | 3.59E-04 | 0.91 | 0.97 | 0.94 |
| Fluo-N2DL-HeLa02 | 167 | 27 | 42 | 1.09E-03 | 0.80 | 0.86 | 0.83 |
| RPE1-01 | 17 | 4 | 2 | 4.47E-04 | 0.9 | 0.81 | 0.71 |
| RPE1-02 | 15 | 4 | 3 | 6.62E-04 | 0.83 | 0.79 | 0.81 |
| RPE1-03 | 27 | 4 | 3 | 6.57E-04 | 0.90 | 0.87 | 0.89 |
| Fluo-N2DH-SIM+01 | 20 | 0 | 8 | 0 | 0.71 | 1 | 0.83 |
| Fluo-N2DH-SIM+02 | 38 | 3 | 6 | 1.01E-0.3 | 0.86 | 0.93 | 0.89 |
| Fluo-N3DH-SIM+01 | 14 | 0 | 23 | 0 | 0.38 | 1 | 0.55 |
| Fluo-N3DH-SIM+02 | 23 | 0 | 17 | 0 | 0.58 | 1 | 0.73 |
| HeLa01-Discs | 82 | 3 | 12 | 3.59E-03 | 0.87 | 0.96 | 0.92 |
| HeLa01-Tracking* | 94 | 59 | 0 | 6.30E-03 | 1 | 0.61 | 0.76 |
| HeLa01-Fusion | 88 | 3 | 6 | 3.59E-04 | 0.94 | 0.97 | 0.95 |

$F_1$ = F-measure, and $P$ = precision.

* HeLa01-Tracking refers to FR-Ro-GE and is not our method.

**Table 2.** Final mitotic detection performance: Results of our algorithm for the datasets detailed in Section 4.1. The above scores refer to both mitosis detection and mother-daughters association. RPE1-01 results are reported for 10-minute sampling rate and RPE1-02, RPE1- 03 for 15 minutes. HeLa01-Discs refers to the proposed method where cells' segmentations are replaced with discs. HeLa01-Tracking refers to a tracking-based mitosis detection of the adapted FR-Ro-GE method that competed in the cell tracking challenge. HeLa01-Fusion refers to the tracking-based detection using our mitosis candidates as anchors.

#### 4.3.5 Tracking-based detection

We next conducted an experiment in which we show that the proposed mitotic events' candidates can be used as anchors in cell tracking algorithms and therefore can enhance cell-lineage analysis by reducing the number of false positive detections (see Fig. A.5 in the Appendix). The last two rows in Table 2 present tracking-based mitosis detection results for the HeLa01 **train** data set obtained by adapting the code of the FR-Ro-GE group, which participated in the cell tracking challenge (Ulman *et al.*, 2017), to mitosis detection (termed here **HeLa01-Tracking**) and by integrating the proposed mitotic events detection with the FR-Ro-GE tracking (**HeLa01-Fusion**). The performances (in terms of $FP$ and $F_1$ scores) of the combined approach are better than each of the methods separately. Fig. A.5 (see Appendix) visually presents false-positive mitosis detection examples obtained using an adapted version of the FR-Ro-GE code. For an additional (approximate) comparison, the reader is referred to the $F_1$ scores (BC measures) of the top three challenge participant methods for the HeLa **test** dataset reported in (Ulman *et al.*, 2017).

#### 4.3.6 Frame rate and spatial resolution influence

We next examined the influence of the frames' spatial resolution and the sequences' temporal resolution on the mitosis detection performances. Scores (TPR, precision and $F_1$ ) for the two experiments, were calculated for each of the three RPE1 sequences and were then averaged. Fig. 7a presents the results obtained for the RPE1 sequences, following spatial down-sampling (using bicubic interpolation) by factors of $1.333, 2, 3,$ and $4$ with respect to the original spatial resolution. We note that the degradation in performances due to downscaling is less significant than expected, possibly since the downsampling functions as a low-pass filter, therefore increasing the frames' signal-to-noise ratio (SNR). Fig. 7b presents the results obtained for the RPE1 sequences, following temporal down-sampling with respect to the original 5-minute frame-rate sequence, simulating frame rates of $10, 15, 20, 25,$ and $30$ minutes. Note that there is a tradeoff between high-frame rate sequences that allow capturing mitotic events right after division (when the daughter cells appear to be identical to each other) and low-frame-rate sequences in which the detected branching (or splitting) points are not ambiguous.

#### 4.3.7 Runtime

Table 3 presents the average run times per frame of the sequences tested. We ran our experiments on i5-6600K, 3.5GHz CPU, 48 GB RAM, 64-bit OS. Reported runtimes for RPE1 data sets are for the full, original sequences acquired every five minutes with the original, full spatial resolution. Reported numbers of cells are estimated based on connected components analysis of the given input segmentations. We note that the initial phase of patch extraction and mitosis candidates identification takes around $90\%$ of the runtime as it applied to the entire population. Solving the integer programing optimization problem takes less than $0.5\%$ of the total runtime.

## 5 Conclusion and future directions

Mitotic cells are a minority with respect to the entire cell population. This imbalance makes supervised mitosis detection techniques, which require annotated data of both mitotic and non-mitotic classes, impractical. The current work takes a different approach, which is fully unsupervised, considering generally applicable spatial and temporal features, characterizing mitosis in microscopy sequences. Specifically, we assume that most cell divisions are symmetrical and are accompanied with local spatio-temporal differences.

The proposed algorithm achieves promising results for different time-lapse fluorescence microscopy sequences and for different temporal and spatial resolutions even though no annotated examples were used and no parameters tuning was applied. Moreover, mother-daughters association does not relay on tracking. This is accomplished via two contributions: stochastic Delaunay triangulation to encode cells' neighborhood and solving the two-to-one integer programming optimization problem to resolve contradicting mother-daughters' triplets. Being independent of frame-to-frame cell association, the proposed mitosis detection framework can be used to boost cell tracking algorithms, where the detected mitotic events serve as anchors for track initialization and termination. Moreover, mitosis detection by itself can be used for the study of phenomena involving periodic and non-periodic changes in proliferation rate.

We should note that there is no assumption made on the dimension of the data. The only adaptation required, when considering 3D frames, relates to the extraction of the daughters' symmetry axis. In the current framework we assumed planar cell division symmetry. General cell division in the 3D space can be addressed by performing 3D similarity transformation between the daughter cells. Moreover, there is no inherent limitation to fluorescently stained cell nuclei and the algorithm can be applied to whole-cell stained data given that the input segmentation accurately extracts both nucleus and cytoplasm and separates individual cells. While none of the underlying assumptions particularly relates to fluorescence microscopy, the labeling facilitates the detection process, highlighting differences and similarities. Furthermore, the condition that each cell is correctly represented by a single connected component cannot be fully satisfied when cells' boundaries cannot be easily distinguished. Therefore, extension to other types of microscopy data acquisition, such as differential interference contrast (DIC) microscopy, requires further study.

Analyzing sensitivity results reveals that in some cases, the same true mitotic daughters are detected more than once. In other cases, very similar adjacent non-mitotic cells are falsely detected. To address both scenarios, future work would expand the proposed optimization by taking into consideration the typical dynamics of cell movement post-mitosis, such as the anti-correlation between sister cells in their direction of motion.

## Acknowledgements

T. Gilad and T. Riklin Raviv would like to thank Nir Drayman, Uri Alon Lab, Weizmann Institute of Science, for a fruitful discussion. T. Gilad and T. Riklin Raviv acknowledge Anne Carpenter and Mark-Anthony Bray, Imaging Platform, The Broad Institute of Harvard and MIT for the MCF-10A dataset segmentations and mitotic events' annotations. G. Lahav acknowledges S.J. Elledge for sharing the RPE hTERT cell line. This study was partially supported by The Israel Science Foundation (T.R.R. 1638/16); Israel Ministry of Science, Technology and Space (T.R.R. 63551). CONACyT/Fundacion Mexico en Harvard(J.R) and Harvard Merit Fellowship (J.R.). The National Institutes of Heath ( NIH GM083303, NIH GM116864 G.L and J.R.), (NIH P50, GM107618 J-Y.C.).

## References

Abdullah (1990). On a robust correlation coefficient. *The Statistician*, pages 455–460.

Alberts *et al.* (2015). *Molecular Biology of the Cell*. Garland Science, New York.

Arbelle, A., Reyes, J., Chen, J.-Y., Lahav, G., and Raviv, T. R. (2018). A probabilistic approach to joint cell tracking and segmentation in high-throughput microscopy videos. *Medical image analysis*, **47**, 140–152.

Bezdek and Dunn (1975). Optimal fuzzy partitions: A heuristic for estimating the parameters in a mixture of normal distributions. *IEEE TC*, **100**(8), 835–838.

Bise, R., Yin, Z., and Kanade, T. (2011). Reliable cell tracking by global data association. In *ISBI*, pages 1004–1010.

Chen *et al.* (2016). Automated mitosis detection with deep regression networks. In *IEEE ISBI*, pages 1204–1207. IEEE.

de Berg *et al.* (2008). *Computational geometry: Algorithms and applications*. Springer, 3rd edition.

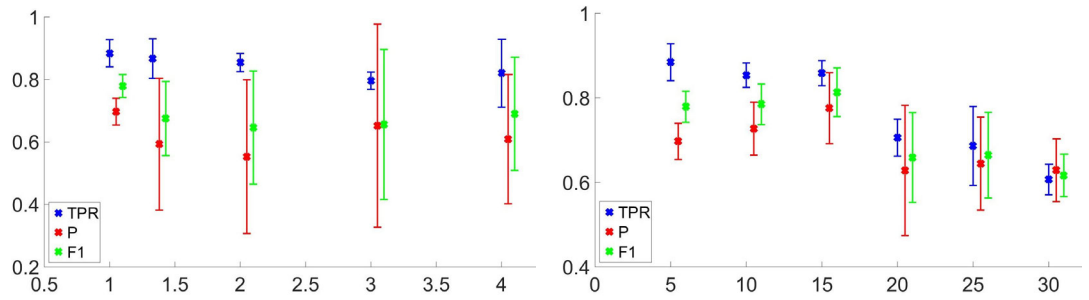


(a) Spatial down-sampling [downscale factor] (b) Temporal down-sampling [frame rate in minutes]

**Fig. 7.** Spatial and temporal downsampling Average scores ($TPR$, $precision$ and $F1$ ) of the three RPE1 sequences that were (a) spatially down-sampled (using bicubic interpolation) by factors of $1.333$, $2$, $3$, and $4$ with respect to the original spatial resolution and (b) temporally down-sampled by factors of $2$, $3$, $4$, $5$, and $6$ with respect to the original sequence, acquired in a rate of 5 minutes per frame. See text for further details.

| Sequence | MCF-10A | HeLa01 | HeLa02 | RPE1(1) | RPE1(2) | RPE1(3) | SIM+2D(1) | SIM+2D(2) | SIM+3D(1) | SIM+3D(2) |
|---|---|---|---|---|---|---|---|---|---|---|
| #frames | 141 | 92 | | 192 | | | 65 | 150 | 150 | 80 |
| frame size [pxls] | $500\times400$ | $1100\times700$ | | $1024\times1024$ | | | $628\times690$ | $739\times773$ | $639\times349\times59$ | $652\times642\times59$ |
| frame rate [fph] | 3 | 3 | | 12 | | | 2 | | 2 | |
| total number of cells | 8178 | 9401 | 28265 | 19606 | 20442 | 20663 | 2594 | 3357 | 2830 | 3261 |
| avg cells per frame | 58 | 102 | 307 | 102 | 107 | 108 | 40 | 22 | 19 | 41 |
| runtime per frame [sec] | 24.91 | 120.9 | 421.0 | 35.45 | 33.26 | 32.46 | 31.42 | 24.19 | 18.0 | 65.22 |

**Table 3. Average run times per frame, frame rate [fph] and spatial resolution for the sequences tested**. Reported runtimes for RPE1 data sets are for the full, original sequences acquired every five minutes with the original, full spatial resolution. Reported numbers of cells are estimated based on connected components analysis of the given input segmentations. HeLa refers to Fluo-N2DL-HeLa dataset. SIM+2D and SIM+3D refer to Fluo-N2DH-SIM+ and Fluo-N3DH-SIM+, respectively.


Delaunay (1934). Sur la sphere vide. *Bulletin de l'Academie des Sciences de l'URSS, Classe des sciences mathematiques et naturelles*, **6**, 793–800.

Dempster *et al.* (1977). Maximum likelihood from incomplete data via the em algorithm. *Journal of the royal statistical society. Series B (methodological)*, pages 1–38.

Dogra *et al.* (2017). Opposite effects of activin type 2 receptor ligands on cardiomyocyte proliferation during development and repair. *Nature communications*, **8**(1), 1902.

Downey *et al.* (2011). Extracting fluorescent reporter time courses of cell lineages from high-throughput microscopy at low temporal resolution. *PloS one*, **6**(12), e27886.

Gath and Geva (1989). Unsupervised optimal fuzzy clustering. *IEEE TPAMI*, **11**(7), 773–780.

Gilad *et al.* (2015). Symmetry-based mitosis detection in time-lapse microscopy. In *IEEE ISBI*, pages 164–167.

Hein *et al.* (2017). Distinct kinetics of serine and threonine dephosphorylation are essential for mitosis. *Nature cell biology*, **19**(12), 1433.

Huh *et al.* (2012). Mitosis detection of hematopoietic stem cell populations in time-lapse phase-contrast microscopy images. In *IEEE ISBI*, pages 390–393. IEEE.

Jablonski *et al.* (2015). Principal component reconstruction error for hyperspectral anomaly detection. *IEEE GRSL*, **12**(8), 1725–1729.

Kamentsky, L., Jones, T. R., Fraser, A., Bray, M. A., Logan, D. J., Madden, K. L., Ljosa, V., Rueden, C., Eliceiri, K. W., and Carpenter, A. E. (2011). Improved structure, function, and compatibility for cellprofiler: modular high-throughput image analysis software. *Bioinformatics*, **7**(8).

Li *et al.* (2010). Multiple nuclei tracking using integer programming quantitative cancer cell cycle analysis. *IEEE TMI*, **29**(1), 96–105.

Liu *et al.* (2010). Automated tracking of stem cell lineages of arabidopsis shoot apex using local graph matching. *The Plant Journal*, **62**(1), 135–147.

Liu *et al.* (2011). Adaptive cell segmentation and tracking for volumetric confocal microscopy images of a developing plant meristem. *Molecular plant*, **4**(5), 922–931.

Liu *et al.* (2012). A semi-markov model for mitosis segmentation in time-lapse phase contrast microscopy image sequences of stem cell populations. *IEEE TMI*, **31**(2), 359–369.

Liu *et al.* (2016). Robust plant cell tracking using local spatio-temporal context. *Neurocomputing*, **208**, 309–314.

Liu *et al.* (2017a). Multi-grained random fields for mitosis identification in time-lapse phase contrast microscopy image sequences. *IEEE TMI*.

Liu *et al.* (2017b). Plant cell tracking using kalman filter based local graph matching. *Image and Vision Computing*, **60**, 154–161.

Magnusson, K., Jalden, J., Gilbert, P., and Blau, H. (2015). Global linking of cell tracks using the viterbi algorithm. *IEEE Transactions on Medical Imaging*, **34**(4), 911–929.

Maska *et al.* (2014). A benchmark for comparison of cell tracking algorithms. *Bioinformatic*, **30**(11), 1609–1617.

Merouane *et al.* (2015). Automated profiling of individual cell–cell interactions from high-throughput time-lapse imaging microscopy in nanowell grids (timing). *Bioinformatics*, **31**(19), 3189–3197.

Nemhauser and Wolsey (1989). Chapter vi integer programming. *Handbooks in Operations Research and Management Science*, **1**, 447–527.

Nie *et al.* (2016). 3d convolutional networks-based mitotic event detection in time-lapse phase contrast microscopy image sequences of stem cell populations. In *Proceedings of the IEEE CVPRW*, pages 55–62.

Otsu (1979). A threshold selection method from gray-level histograms. *IEEE transactions on systems, man, and cybernetics*, **9**(1), 62–66.

Pearson (1895). Note on regression and inheritance in the case of two parents. *Proceedings of the Royal Society of London*, **58**, 240–242.

Phan *et al.* (2017). An unsupervised long short-term memory neural network for event detection in cell videos. *arXiv preprint arXiv:1709.02081*.

Pohl *et al.* (2006). Logarithm odds maps for shape representation. In *International Conference on Medical Image Computing and Computer-Assisted Intervention*, pages 955–963. Springer.

Powers (2011). Evaluation: from precision, recall and f-measure to roc, informedness, markedness and correlation. *Journal of Machine*

*Learning Technologies*.

Riklin Raviv *et al.* (2009). On symmetry, perspectivity, and level-set based segmentation. *IEEE TPAMI*, **31**(8), 1458–1471.

Riklin Raviv *et al.* (2010). Segmentation of image ensembles via latent atlases. *Medical Image Analysis*, **14**(5), 654–665.

Roux *et al.* (2013). Mitosis detection in breast cancer histological images an icpr 2012 contest. *Journal of pathology informatics*, **4**.

Roux *et al.* (2014). Mitos & atypia. *Image Pervasive Access Lab, Agency Sci., Technol. & Res. Inst. Infocom Res., Singapore, Tech. Rep*, **1**.

Sullivan, D. and Epstein, W. (1963). Mitotic activity of wounded human epidermis. *J Invest Dermatol.*

Svoboda, D. and Ulman, V. (2017). MitoGen: A framework for generating 3d synthetic time-lapse sequences of cell populations in fluorescence microscopy,. *IEEE Transactions on Medical Imaging*, **36**(1), 310–321.

Tashk *et al.* (2015). Automatic detection of breast cancer mitotic cells based on the combination of textural, statistical and innovative mathematical features. *Applied Mathematical Modelling*, **39**(20), 6165–6182.

Thirusittampalam *et al.* (2013). A novel framework for cellular tracking and mitosis detection in dense phase contrast microscopy images. *IEEE J. Biomedical and Health Informatics*, **17**(3).

Tonti *et al.* (2015). Unsupervised hep-2 mitosis recognition in indirect immunofluorescence imaging. In *IEEE EMBC*, pages 8135–8138. IEEE.

Ulman, V., Maška, M., Magnusson, K., Ronneberger, O., *et al.* (2017). An objective comparison of cell tracking algorithms. *Nature Methods*, **14**(12), 1141–1152.

Vergassola, M., Deneke, V., and Di Talia, S. (2018). Mitotic waves in the early embryogenesis of drosophila: Bistability traded for speed. *Proc Natl Acad Sci*, **115**(10), E2165–E2174.

Veta *et al.* (2015). Assessment of algorithms for mitosis detection in breast cancer histopathology images. *Medical image analysis*, **20**(1), 237–248.

Wan *et al.* (2017). Automated mitosis detection in histopathology based on non-gaussian modeling of complex wavelet coefficients. *Neurocomputing*, pages 291–303.

Zimmer *et al.* (2006). On the digital trail of mobile cells. *IEEE Signal Processing Magazine*, **23**(3), 54–62.